

First Search for Ultralight Dark Matter Using a Magnetically Levitated Particle

Dorian W. P. Amaral ^{1,*}, Dennis G. Uitenbroek ², Tjerk H. Oosterkamp ² and Christopher D. Tunnell ¹

¹*Department of Physics and Astronomy, Rice University, MS-315, Houston, TX, 77005, U.S.A.*

²*Leiden Institute of Physics, Leiden University, P.O. Box 9504, 2300 RA Leiden, The Netherlands.*

We perform the first search for ultralight dark matter using a magnetically levitated particle. A sub-millimeter permanent magnet is levitated in a superconducting trap with a measured force sensitivity of $0.2 \text{ fN}/\sqrt{\text{Hz}}$. We find no evidence of a signal and derive limits on dark matter coupled to the difference between baryon and lepton number, $B - L$, in the mass range $(1.10360 - 1.10485) \times 10^{-13} \text{ eV}/c^2$. Our most stringent limit on the coupling strength is $g_{B-L} \lesssim 2.98 \times 10^{-21}$. We propose the POLONAISE (Probing Oscillations using Levitated Objects for Novel Accelerometry in Searches of Exotic physics) experiment, featuring short-, medium-, and long-term upgrades that will give us leading sensitivity in a wide mass range and demonstrating the promise of this novel quantum sensing technology in the hunt for dark matter.

Introduction.—Dark matter (DM) dominates the matter content of our Universe. Yet, we know remarkably little about its fundamental nature. Except for the fact that it must interact gravitationally, important properties such as its mass, spin, and other potential interactions remain largely a mystery [1–3]. Astrophysical observations suggest that its mass can lie anywhere in the range of $10^{-19} \text{ eV}/c^2$ to a few solar masses, spanning a vast 90 orders of magnitude [4, 5]. The lower end of this mass window defines the *ultralight* regime for dark matter, which has been gaining considerable attention [6].

In this regime, ultralight dark matter (ULDM) particles must be bosonic to reconcile the observed dark matter density. A consequence of this is that these particles exhibit wavelike behavior, giving rise to interference regions throughout the cosmos. Popular ultralight candidates include the QCD axion [7–9], axion-like particles as well as other scalars [10–12], and—of relevance to us—vector particles [13–15].

Ultralight vector dark matter particles are spin-1 bosons that stem from the same type of symmetry as the Standard Model photon. Many early-Universe production mechanisms lead to this type of dark matter [16–26], and the late-Universe structures that it can form have been explored via numerical simulations [27–31]. These particles can communicate with us via charges different from that of electromagnetism. In this work, we take this to be the difference between the baryon and lepton numbers of a particle, $B - L$; this leads to a well-motivated dark matter candidate [32, 33] that can also serve to explain the non-zero mass of the neutrino [34–36].

Many experiments have constrained the interaction strength of $B - L$ coupled dark matter, and a variety of detector technologies have been used to derive projected sensitivities. Limits have been set by fifth-force experiments, such as MICROSCOPE [37–40] and Eöt-Wash [41, 42], and gravitational wave interferometers, such as LIGO/Virgo [43] and KAGRA [44], among other experiments. Projections with accelerometers have been shown to be particularly promising [45, 46], with these instruments being realized as torsion balances [45], optome-

chanical cavities [47, 48], atomic interferometers [49], and future gravitational-wave detectors [50–53].

One detector technology currently undergoing a significant rate of innovation involves the levitation of macroscopic objects via magnetic Meissner levitation [54–56]. The low temperatures involved in these setups provide exceptionally low thermal noise and, compared to optical levitation strategies, much larger levitated objects are possible [54]. Levitated magnets are excellent force and acceleration sensors [57, 58], making them ideal for detecting the minuscule signatures expected from ultralight dark matter [59–61].

In this Letter, we perform the first search for ultralight dark matter using a magnetically levitated mass and propose the POLONAISE (Probing Oscillations using Levitated Objects for Novel Accelerometry in Searches of Exotic physics) experiment. We analyze data from the setup initially described in Ref. [57] for tests of small-scale gravity, employing a sub-millimetre-sized magnetically levitated particle. Using a likelihood-led treatment to perform our inferencing, we account for the inherent stochasticity in the ULDM field. We offer a set of short-, medium-, and long-term upgrades to form POLONAISE, which will allow us to achieve leading sensitivity to ULDM and highlight the advancements in quantum metrology necessary for a world-leading DM experiment.

Ultralight vector dark matter.—Ultralight vector dark matter consists of spin-1 bosons with masses m_{DM} approximately between $10^{-19} \text{ eV}/c^2$ to $2 \text{ eV}/c^2$ [12]. To make up all of the local dark matter density, $\rho_{\text{DM}} \approx 0.4 \text{ GeV}/c^2 \text{ cm}^{-3}$ [62, 63], their small mass results in a macroscopic number of particles within a de Broglie volume, λ_{dB}^3 . Assuming virialization and taking the local circular velocity to be $v_0 \approx 220 \text{ km s}^{-1}$ [64], we have a total of $N_{\text{dB}} \sim (\rho_{\text{DM}}/m_{\text{DM}})(h/m_{\text{DM}}v_0)^3 \sim 10^{58}$ particles for a DM mass of $10^{-13} \text{ eV}/c^2$. A consequence of this is that DM particles within the halo behave more like waves than particles.

Within a de Broglie volume, these DM waves oscillate coherently at their Compton angular frequency

$\omega_{\text{DM}} \equiv 2\pi f_{\text{DM}} = m_{\text{DM}}c^2/\hbar$, with a small frequency spread of $\Delta\omega \simeq (v_0^2/c^2)\omega_{\text{DM}} \sim 10^{-6}\omega_{\text{DM}}$ between volumes. These define coherent regions that travel at an average velocity of v_0 , with coherence maintained over the timescale $\tau_{\text{coh}} \equiv \lambda_{\text{dB}}/v_0 = h/(m_{\text{DM}}v_0^2) \approx 21$ h for a DM mass of 10^{-13} eV/ c^2 . We remain in the coherent regime throughout this work.

Within this regime, the ultralight vector DM field at time t , $\mathbf{A}(t)$, traces out a three-dimensional ellipse. It can be written as [40, 65]

$$\mathbf{A}(t) = \frac{\hbar}{m_{\text{DM}}c^2} \sqrt{\frac{2\rho_{\text{DM}}}{3\varepsilon_0}} \sum_i \alpha_i \cos(\omega_{\text{DM}}t + \varphi_i) \hat{\mathbf{e}}_i, \quad (1)$$

where ε_0 is the permittivity of free space, and the sum runs over the three components of the field, $i \in \{x, y, z\}$. The parameters α_i and φ_i respectively control the amplitudes and phases of each of the field's components, and they are stochastic. Incorporating the randomness in these variables is crucial for accurate inferences, as this can lead to significant correction factors [52, 66–68].

The ultralight vector dark matter field generates new electric and magnetic fields that can couple to ordinary matter. For non-relativistic ULDm, the electric field dominates and results in a new Lorentz force, $\mathbf{F}(t)$. For simplicity, we consider the force aligned along a single axis, ζ , such that the relevant force is $F_{\text{DM}}(t) \equiv \zeta \cdot \mathbf{F}(t)$. Since our observation time, T_{obs} , is shorter than a day, we approximate ζ to be static and aligned along the zenith. Accounting for the dynamics of the trap and levitated particle, the force experienced by the latter is

$$F_{\text{DM}}^p(t) \simeq \mathcal{F} [\alpha_x \cos \lambda \cos \phi \cos(\omega_{\text{DM}}t + \varphi_x) + \alpha_y \cos \lambda \sin \phi \cos(\omega_{\text{DM}}t + \varphi_y) + \alpha_z \sin \lambda \cos(\omega_{\text{DM}}t + \varphi_z)], \quad (2)$$

where we have defined the force scale

$$\mathcal{F} \equiv g_{B-L} \left(\mathcal{R}_p - \frac{\omega_0^2}{\omega_{\text{DM}}^2} \mathcal{R}_t \right) m_p a_0, \quad (3)$$

with g_{B-L} the gauge coupling strength of the field, \mathcal{R}_p and \mathcal{R}_t the averaged neutron-to-atomic-weight ratios of the particle and trap, respectively, ω_0 the resonance angular frequency of the particle, m_p the total mass of the levitated particle, and $a_0 \approx 2.12 \times 10^{11} \text{ ms}^{-2}$ a characteristic acceleration imparted by the ULDm field per nucleon [65].

We perform inferences in Fourier space by analyzing the force power spectral density (PSD). The PSD will contain the power delivered to our setup by external sources, as well as that supplied by a potential ULDm signal. When observing for less than a day, this signal manifests as a monochromatic peak in the PSD within the bin containing the Compton frequency. The quantity of interest for our inferring is the *excess power* at that

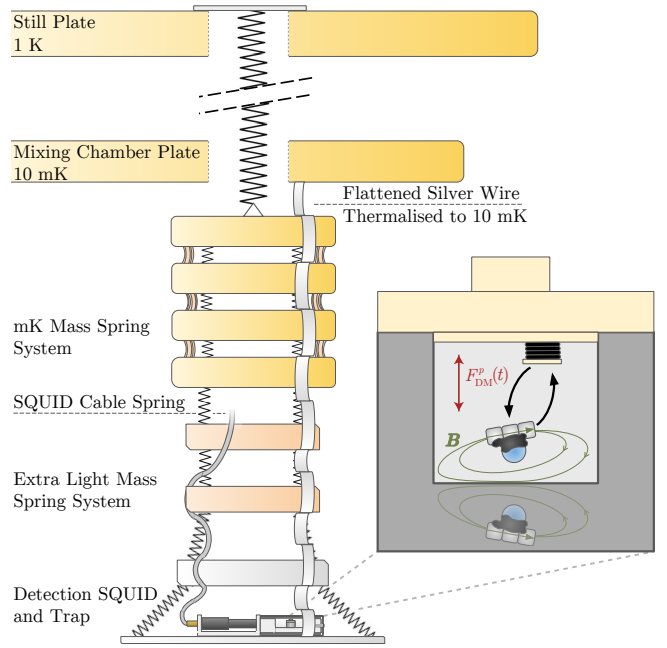


FIG. 1: Schematic of the experimental setup inside the dilution refrigerator. Shown are the plates of the cryostat, the multi-stage mass-spring system used to shield against external vibrations, and the holder for the trap and magnet. The inset shows the superconducting trap containing the magnet. The \mathbf{B} -field, which cannot enter the superconductor due to the Meissner effect, can be modelled by an image dipole, causing the magnet to levitate. The oscillatory force imparted by the ULDm field, $F_{\text{DM}}^p(t)$ as given in Eq. (2), is also indicated. The black arrows illustrate the coupling of the flux of the moving particle to the pickup coil. Further details and photographs of the setup can be found in Ref. [57].

frequency, defined as the value of the PSD normalized by the expected noise, S_{FF} , within that bin. The excess power is proportional to the square of the dimensionless parameter [65]

$$\kappa \equiv \sqrt{\frac{\mathcal{F}^2 T_{\text{obs}}}{2S_{FF}}}, \quad (4)$$

with \mathcal{F} given in Eq. (3). By measuring the force PSD and fitting to our expected noise level, we perform inferences on κ and map these values to those for the coupling strength, g_{B-L} :

$$g_{B-L} = \frac{\kappa}{|\mathcal{R}_p - (\omega_0^2/\omega_{\text{DM}}^2)\mathcal{R}_t| m_p a_0} \sqrt{\frac{2S_{FF}}{T_{\text{obs}}}}. \quad (5)$$

Experiment.—Originally designed to detect small-scale gravity [57], our setup has the force sensitivity and frequency range required of a promising ULDm detector.

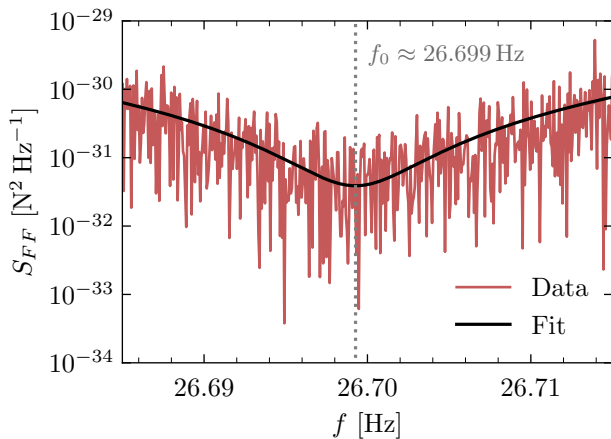


FIG. 2: The force power spectral density, S_{FF} , with frequency f measured by our experiment. The fit to the force noise background via Eq. (6) is also shown. The vertical line highlights the resonance frequency $f_0 \approx 26.699$ Hz relevant for motions parallel to the zenith. Data initially reported in Ref. [57].

It features a Type-I superconducting trap with a magnetically levitated permanent magnet composed of three 0.25 mm $\text{Nd}_2\text{Fe}_{14}\text{B}$ cubes and a spherical glass bead of radius 0.25 mm to break rotational symmetry (Fig. 1). The levitated particle has a mass of $m_p \approx 0.43$ mg, a resonance frequency of $f_0 \approx 26.7$ Hz for motions along the zenith, and a quality factor of $Q \approx 9.3 \times 10^6$ [57]. We calculate the particle averaged neutron-to-atomic-weight ratio to be $\mathcal{R}_p \approx 0.517$.

We detect the motion of the particle using a superconducting pick-up loop at the top of the trap. The motion of the magnet induces a change in flux in the loop, causing a superconducting current to run in the circuit. This circuit consists of the pick-up loop, the calibration loop, and the SQUID input coil, which is inductively coupled to a two-stage direct current SQUID. The calibration loop calibrates the energy coupling, β^2 , between the detection circuit and the degrees of motion of the magnet. We find the averaged neutron-to-atomic-weight ratio of the trap, including its magnetic shielding, to be $\mathcal{R}_t \approx 0.526$.

We shield the trap from environmental vibrations both vertically and laterally using a multi-stage mass-spring system, and we thermalize the experiment via a flexible silver wire. The closest part of this system, consisting of seven masses, hangs from the still plate, which is suspended from the 3 K plate of the cryostat. The cryostat rests on a 25-ton concrete block with pneumatic dampers to reduce vibrations caused by the building. The pulse tube cooler and vacuum pumps are mounted separately. Further details are included in Ref. [57].

The force noise data gathered in Ref. [57] is shown in Fig. 2. The data was continuously recorded on 13th May, 2022 over a time of $T_{\text{obs}} \approx 4.2$ h between

22:32 and 02:44 UTC and spans the frequency range 26.6850 Hz–26.7150 Hz. Compared to the original data, we have removed two points: one at the frequency of a produced monochromatic signal (a spinning wheel used for a gravity test) and another at the resonance frequency. The latter was done because the ringdown time of the resonator exceeded the dataset length, so this point represented the starting amplitude of the resonator (see supplement E of Ref. [57]). We fit the data to the total expected force noise via

$$S_{FF}(\omega) = S_{FF}^0 + |\chi(\omega)|^{-2} S_{xx}, \quad (6)$$

where S_{FF}^0 is the force noise arising from the position measurement of the particle, and S_{xx} is the displacement noise due to measurement-added noise from the SQUID. The factor $\chi(\omega) \equiv [m_p(\omega_0^2 - \omega^2 + i\gamma\omega)]^{-1}$ is the mechanical susceptibility, with $\omega_0 \equiv 2\pi f_0$ and $\gamma \equiv \omega_0/Q$. We find the fit values $S_{FF}^0 \approx 3.88 \times 10^{-32} \text{ N}^2 \text{ Hz}^{-1}$ and $S_{xx} \approx 3.59 \times 10^{-21} \text{ m}^2 \text{ Hz}^{-1}$. We use this fit in Eq. (4) when making inferences on κ and, ultimately, on g_{B-L} .

Data analysis and results.—The ULDM signal manifests as a monochromatic peak in the force PSD within the bin containing the Compton frequency, f_{DM} . Its location is dictated by the DM mass, and its noise-normalized amplitude is determined by the dimensionless parameter κ , defined in Eq. (4). We scan over our frequency bins, equivalent to scanning over dark matter masses m_{DM} , and use our measured force PSD to make inferences on the coupling strength, g_{B-L} .

To perform our search, we follow a frequentist, likelihood-based approach similar to Ref. [40]. The likelihood of measuring a value for the excess power in any frequency bin is a non-central χ^2 with two degrees of freedom and a non-centrality parameter controlled by κ . To account for the stochasticity of the ULDM field, we marginalize this likelihood over the three random Rayleigh amplitudes and uniform phases. The result is an exponential likelihood with inverse scale $2 + \kappa^2$ [65].

We use this likelihood to define a two-sided test statistic (TS) based on the log-likelihood ratio to ascertain whether a DM signal is present. As our discovery criterion, we require that the excess power yields at least a 3σ significance over the expected background, equivalent to a p -value of 2.7×10^{-3} . We evaluate this by first building the distribution of the TS under the null hypothesis that no such signal exists using toy Monte Carlo (MC) simulations. At every frequency bin, we then compute the p -value of the data. Our most significant local p -value is $p \approx 2.0 \times 10^{-2}$, which does not exceed our discovery threshold. We therefore turn to setting a limit.

We place 90% confidence level (CL) limits on g_{B-L} using a similar procedure, but taking the signal hypothesis as our null hypothesis. To assess whether our limit is consistent with that from background-only data, we also derive the expected median limit and $1\sigma/2\sigma$ limit bands

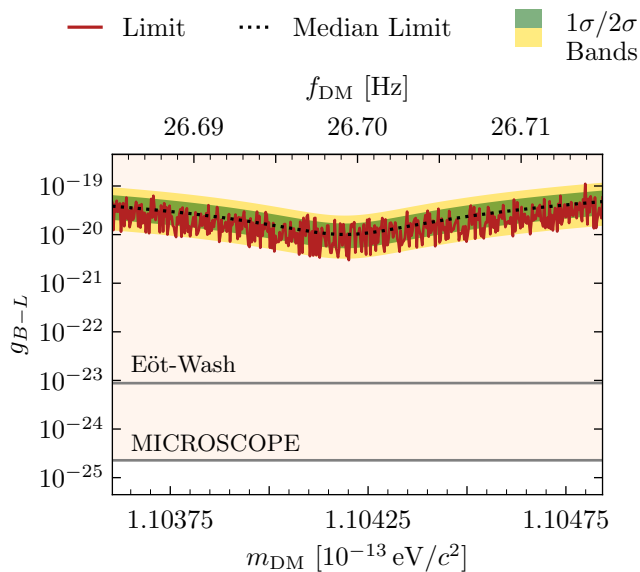


FIG. 3: The 90% confidence level limits on the gauge coupling strength g_{B-L} with dark matter mass m_{DM} (bottom axis) and Compton frequency f_{DM} (top axis). Shown is the data-driven limit derived from the measurements presented in Fig. 2, as well as the median limit and $1\sigma/2\sigma$ bands derived from our Monte Carlo analysis [65]. Also shown are the existing limits from the Eöt-Wash [41, 42] and MICROSCOPE [39, 40] experiments.

from our setup by simulating background-only pseudo-data and repeating the above procedure for each dataset. We find $\kappa_{\text{lim}}^{\text{med}} \approx 3.85$, with 1σ and 2σ bands given by $\kappa_{\text{lim}}^{1\sigma} \in [2.01, 6.47]$ and $\kappa_{\text{lim}}^{2\sigma} \in [1.23, 9.39]$, respectively. We do not show the lower limits arising from our two-sided TS construction since we cannot claim a discovery, instead quoting only the upper limits. Further details on our statistical procedure can be found in Ref. [65].

We show our 90% CL limit in Fig. 3. We find excellent agreement between the results from our MC analysis and our derived data-driven limit, which closely follows the median limit and lies well within the 2σ band. Our best constraint is $g_{B-L} \lesssim 2.98 \times 10^{-21}$, occurring at the DM mass $m_{DM} \approx 1.1042 \times 10^{-13} \text{ eV}/c^2$ (Compton frequency $f_{DM} \approx 26.6995 \text{ Hz}$). This limit is not as stringent as those set by the fifth-force Eöt-Wash [41, 42] and MICROSCOPE [39, 40] experiments, falling at $g_{B-L} \lesssim 10^{-23}$ and $g_{B-L} \lesssim 2 \times 10^{-25}$, respectively.

Our limit is the first data-driven constraint on ultra-light dark matter using a magnetically levitated particle. However, we derived it using a setup originally designed for tests of gravity—an orthogonal research objective [57]. To go further, we offer a set of experimentally-driven upgrades that will make this detector technology a leading option in the search for dark matter, proposing the POLONAISE experiment.

Future Prospects.—We propose the first optimization of a magnetically-levitated setup to achieve leading ULDM sensitivities with POLONAISE. Our key improvement is adding a second coil to control the resonant frequency, allowing us to probe a wider DM mass range. To maximize sensitivity to smaller g_{B-L} values, we aim to reduce force noise, use heavier levitated masses, and increase the neutron-to-atomic-weight ratio difference between the particle and trap. We plan to perform a two-year-long resonant scan with short-, medium-, and long-term upgrades, summarized in Table I. We estimate these upgrades will take 3, 5 and 10 years to develop the required technology, respectively. Further details on our choices can be found in Ref. [65].

At each resonance frequency, f_0 , we will measure for 4.05×10^5 Compton cycles to ensure coherence, giving $T_{\text{obs}} = 4.05 \times 10^5 / f_0$. We will match our frequency steps to the optimal bandwidth, Δf_{opt} , that maximizes our mass sensitivity while minimizing the amount of noise introduced by tuning the SQUID coupling to have the backaction noise equal to the thermal noise. Cooling will reach 20 mK (short/medium-term) and 2 mK (long-term) using nuclear demagnetization [69]. We will improve the quality factor by using insulating magnets to reduce Eddy current damping [70] and improving SQUID energy resolution with alternating current readouts [71]. Avoiding crosstalk and interference in the SQUID readout will reduce n_{SQ} by factors of 10 (short-term) and 100-1000 (medium/long-term) with radio frequency readouts [56]. A persistent current will be used in the added coil to minimize additional current-added noise [72]. Lastly, we will parallelize our scan by using multiple levitated particles monitored by a single SQUID, with potential scalability to a commercial dilution refrigerator housing up to 100 SQUIDs. In the short term, we will scan a range of 21 Hz–35 Hz, extending this to 10 Hz–200 Hz in the medium and long term.

Exploiting magnetic levitation’s ability to support heavier objects, we plan to improve our sensitivity by increasing the particle mass, with proposed masses of 43 mg (short-term) and 430 mg (medium/long-term). Maintaining force noise and reducing trap vibrations will be challenging as the spring constant, $k_p \propto m_p$, increases with mass. At 25 Hz, our upgrades require vibration isolation improvements of 40 dB, 80 dB, and 100 dB, respectively. This is feasible since the required isolation, needed only at the particle’s resonance frequency, is comparable to LIGO’s performance but over a narrower frequency band [73]. Finally, by optimizing the materials used for the magnetic particle and the trap, we will improve $|\mathcal{R}_p - \mathcal{R}_t|$ to 0.039 (short/medium-term) and 0.213 (long-term). For our long-term goal, we can achieve this by attaching a thin-walled aluminium container filled with 1 liter of solid hydrogen.

Considering our proposed upgrades, we use Eq. (5) to derive the 90% CL projected limits on the coupling

	Short	Medium	Long
T [mK]	20	20	2
m_p [mg]	0.43	430	430
n_{SQ} [\hbar]	10^3	10^2	10^1
$\sqrt{S_{FF}}$ [$\text{N}/\sqrt{\text{Hz}}$]	$10^{-19} f_0^{1/2}$	$10^{-18} f_0^{1/2}$	$10^{-19} f_0^{1/2}$
Δf_{opt} [mHz]	3.4	3.4	0.34
Q	10^8	10^9	10^{10}
$ \mathcal{R}_p - \mathcal{R}_t $	0.039	0.039	0.213
N_p	1	10	100

TABLE I: The short-, medium-, and long-term upgrades we propose for POLONAISE. Shown are the cooling temperature (T), the mass of the levitated particle (m_p), the SQUID energy resolution as a factor (n_{SQ}), the total root force PSD ($\sqrt{S_{FF}}$), the bandwidth that optimizes the expected force noise (Δf_{opt}), the quality factor (Q), the absolute difference between the neutron-to-atomic-weight ratios of the levitated particle and trap ($|\mathcal{R}_p - \mathcal{R}_t|$), and the number of levitated particles employed (N_p). At each resonance frequency, f_0 , the measurement time is given by $T_{\text{obs}} = 4.05 \times 10^5 / f_0$.

strength at each resonance frequency. For this, we use the median value of the dimensionless coupling parameter κ derived from our MC analysis, $\kappa_{\text{lim}}^{\text{med}} \approx 3.85$. This gives us our projected limits on g_{B-L} assuming a background-only measurement, shown in Fig. 4. Our short-term upgrade is competitive with the Eöt-Wash [41, 42] experiment, with our medium- and long-term configurations probing new regions of the ULDM parameter space. Our medium-term limit surpasses that of Eöt-Wash over all of our scanned mass range, is competitive with MICROSCOPE at low masses, and constrains new couplings beyond those of both MICROSCOPE and LIGO/Virgo [42, 43] at high masses. Our long-term configuration produces a leading limit over all of our mass range, going beyond the limit set by MICROSCOPE [39, 40] by two orders of magnitude at lower masses and that set by LIGO/Virgo by three orders of magnitude at higher masses.

Conclusions.—We have performed the first search for ultralight dark matter using a magnetically levitated particle. Focusing on dark matter coupled to the difference between baryon and lepton number, $B - L$, we have found no evidence of a signal in the mass range $(1.10360\text{--}1.10485) \times 10^{-13} \text{ eV}/c^2$, equivalent to the frequency range 26.6850 Hz–26.7150 Hz. We have set a 90% confidence level limit on the coupling strength, finding the best constraint to be $g_{B-L} \lesssim 2.98 \times 10^{-21}$. We have proposed the POLONAISE experiment, featuring short-,

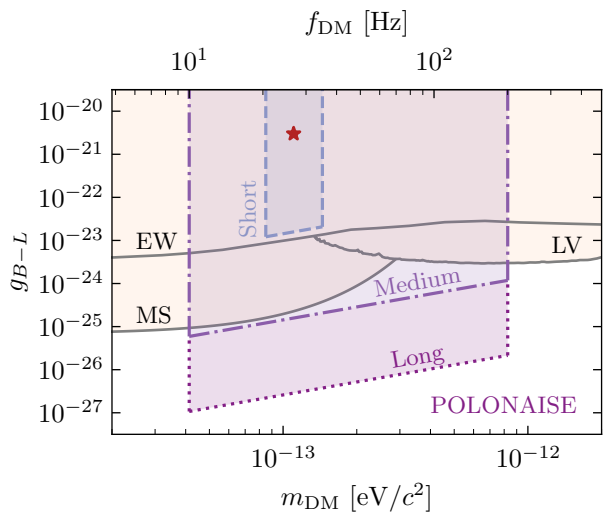


FIG. 4: Projected 90% confidence level limits on the gauge coupling strength g_{B-L} with dark matter mass m_{DM} (bottom axis) and Compton frequency f_{DM} (top axis) for POLONAISE. Projections are based on the short-, medium-, and long-term configurations detailed in Table I. Also shown is our current best limit from Fig. 3 by means of a red star, as well as the existing limits from the MICROSCOPE (MS) [39, 40], Eöt-Wash (EW) [41, 42], and LIGO/Virgo (LV) [42, 43] experiments. The limit from our medium-term setup begins to surpass existing constraints, and that of our long-term configuration is leading by multiple orders of magnitude.

medium-, and long-term improvements to our setup to enable sensitivity to unexplored model parameter space. Our result highlights the promise of this quantum sensing technology in the hunt for dark matter, and we hope that it fuels initiatives in advancing experimental designs of magnetically levitated setups for astroparticle physics.

We would like to thank Daniel Carney, Andrew Long, Bas Hensen, Mudit Jain, Martijn Janse, and Yue Zhao for their valuable feedback on the manuscript. DA would like to thank Juehang Qin for helpful discussions throughout this work, especially concerning our statistical treatment, as well as Mustafa Amin for discussions regarding the ultralight dark matter field. DA and CT were jointly funded by Rice University and NSF award 2046549. TO acknowledges funding from NWO grant OCENW.GROOT.2019.088. DU and TO were jointly funded by the EU Horizon Europe EIC Pathfinder project QuCoM (10032223).

* dorian.amaral@rice.edu

[1] G. Bertone and D. Hooper, “History of dark matter,” *Rev. Mod. Phys.* **90**, 045002 (2018), [arXiv:1605.04909](https://arxiv.org/abs/1605.04909)

- [astro-ph.CO].
- [2] K. Freese, “Status of Dark Matter in the Universe,” *Int. J. Mod. Phys. A* **1**, 325 (2017), arXiv:1701.01840 [astro-ph.CO].
- [3] M. Cirelli, A. Strumia, and J. Zupan, “Dark Matter,” (2024), arXiv:2406.01705 [hep-ph].
- [4] T. D. Brandt, “Constraints on MACHO Dark Matter from Compact Stellar Systems in Ultra-Faint Dwarf Galaxies,” *Astrophys. J. Lett.* **824**, L31 (2016), arXiv:1605.03665 [astro-ph.GA].
- [5] N. Dalal and A. Kravtsov, “Excluding fuzzy dark matter with sizes and stellar kinematics of ultrafaint dwarf galaxies,” *Phys. Rev. D* **106**, 063517 (2022), arXiv:2203.05750 [astro-ph.CO].
- [6] R. Essig *et al.*, “Working Group Report: New Light Weakly Coupled Particles,” in *Snowmass 2013: Snowmass on the Mississippi* (2013) arXiv:1311.0029 [hep-ph].
- [7] S. Weinberg, “A New Light Boson?” *Phys. Rev. Lett.* **40**, 223 (1978).
- [8] F. Wilczek, “Problem of Strong P and T Invariance in the Presence of Instantons,” *Phys. Rev. Lett.* **40**, 279 (1978).
- [9] L. Di Luzio, M. Giannotti, E. Nardi, and L. Visinelli, “The landscape of QCD axion models,” *Phys. Rept.* **870**, 1 (2020), arXiv:2003.01100 [hep-ph].
- [10] A. Arvanitaki, S. Dimopoulos, S. Dubovsky, N. Kaloper, and J. March-Russell, “String Axiverse,” *Phys. Rev. D* **81**, 123530 (2010), arXiv:0905.4720 [hep-th].
- [11] A. Ringwald, “Axions and Axion-Like Particles,” in *49th Rencontres de Moriond on Electroweak Interactions and Unified Theories* (2014) pp. 223–230, arXiv:1407.0546 [hep-ph].
- [12] E. G. M. Ferreira, “Ultra-light dark matter,” *Astron. Astrophys. Rev.* **29**, 7 (2021), arXiv:2005.03254 [astro-ph.CO].
- [13] J. Jaeckel, “A force beyond the Standard Model - Status of the quest for hidden photons,” *Frascati Phys. Ser.* **56**, 172 (2012), arXiv:1303.1821 [hep-ph].
- [14] M. Fabbrichesi, E. Gabrielli, and G. Lanfranchi, “The Dark Photon,” (2020), 10.1007/978-3-030-62519-1, arXiv:2005.01515 [hep-ph].
- [15] A. Caputo, A. J. Millar, C. A. J. O’Hare, and E. Vitagliano, “Dark photon limits: A handbook,” *Phys. Rev. D* **104**, 095029 (2021), arXiv:2105.04565 [hep-ph].
- [16] P. W. Graham, J. Mardon, and S. Rajendran, “Vector Dark Matter from Inflationary Fluctuations,” *Phys. Rev. D* **93**, 103520 (2016), arXiv:1504.02102 [hep-ph].
- [17] P. Agrawal, N. Kitajima, M. Reece, T. Sekiguchi, and F. Takahashi, “Relic Abundance of Dark Photon Dark Matter,” *Phys. Lett. B* **801**, 135136 (2020), arXiv:1810.07188 [hep-ph].
- [18] R. T. Co, A. Pierce, Z. Zhang, and Y. Zhao, “Dark Photon Dark Matter Produced by Axion Oscillations,” *Phys. Rev. D* **99**, 075002 (2019), arXiv:1810.07196 [hep-ph].
- [19] J. A. Dror, K. Harigaya, and V. Narayan, “Parametric Resonance Production of Ultralight Vector Dark Matter,” *Phys. Rev. D* **99**, 035036 (2019), arXiv:1810.07195 [hep-ph].
- [20] M. Bastero-Gil, J. Santiago, L. Ubaldi, and R. Vega-Morales, “Vector dark matter production at the end of inflation,” *JCAP* **04**, 015 (2019), arXiv:1810.07208 [hep-ph].
- [21] A. J. Long and L.-T. Wang, “Dark Photon Dark Matter from a Network of Cosmic Strings,” *Phys. Rev. D* **99**, 063529 (2019), arXiv:1901.03312 [hep-ph].
- [22] E. W. Kolb and A. J. Long, “Completely dark photons from gravitational particle production during the inflationary era,” *JHEP* **03**, 283 (2021), arXiv:2009.03828 [astro-ph.CO].
- [23] R. T. Co, K. Harigaya, and A. Pierce, “Gravitational waves and dark photon dark matter from axion rotations,” *JHEP* **12**, 099 (2021), arXiv:2104.02077 [hep-ph].
- [24] P. Adshead, K. D. Lozanov, and Z. J. Weiner, “Dark photon dark matter from an oscillating dilaton,” *Phys. Rev. D* **107**, 083519 (2023), arXiv:2301.07718 [hep-ph].
- [25] D. Cyncynates and Z. J. Weiner, “Detectable, defect-free dark photon dark matter,” (2023), arXiv:2310.18397 [hep-ph].
- [26] O. Özsoy and G. Tasinato, “Vector dark matter, inflation, and non-minimal couplings with gravity,” *JCAP* **06**, 003 (2024), arXiv:2310.03862 [astro-ph.CO].
- [27] M. A. Amin, M. Jain, R. Karur, and P. Mocz, “Small-scale structure in vector dark matter,” *JCAP* **08**, 014 (2022), arXiv:2203.11935 [astro-ph.CO].
- [28] M. Gorghetto, E. Hardy, J. March-Russell, N. Song, and S. M. West, “Dark photon stars: formation and role as dark matter substructure,” *JCAP* **08**, 018 (2022), arXiv:2203.10100 [hep-ph].
- [29] M. Jain and M. A. Amin, “i-SPin: an integrator for multicomponent Schrödinger-Poisson systems with self-interactions,” *JCAP* **04**, 053 (2023), arXiv:2211.08433 [astro-ph.CO].
- [30] M. Jain, M. A. Amin, J. Thomas, and W. Wanichwecharungruang, “Kinetic relaxation and Bose-star formation in multicomponent dark matter,” *Phys. Rev. D* **108**, 043535 (2023), arXiv:2304.01985 [astro-ph.CO].
- [31] M. Jain, M. A. Amin, and H. Pu, “Integrator for general spin- s Gross-Pitaevskii systems,” *Phys. Rev. E* **108**, 055305 (2023), arXiv:2305.01675 [cond-mat.quant-gas].
- [32] P. Fayet, “Effects of the Spin 1 Partner of the Goldstino (Gravitino) on Neutral Current Phenomenology,” *Phys. Lett. B* **95**, 285 (1980).
- [33] P. Fayet, “On the Search for a New Spin 1 Boson,” *Nucl. Phys. B* **187**, 184 (1981).
- [34] M. E. Peskin and D. V. Schroeder, *An Introduction to quantum field theory* (Addison-Wesley, Reading, USA, 1995).
- [35] L. Basso, A. Belyaev, S. Moretti, and C. H. Shepherd-Themistocleous, “Phenomenology of the minimal B-L extension of the Standard model: Z' and neutrinos,” *Phys. Rev. D* **80**, 055030 (2009), arXiv:0812.4313 [hep-ph].
- [36] S. Kanemura, T. Matsui, and H. Sugiyama, “Neutrino mass and dark matter from gauged $U(1)_{B-L}$ breaking,” *Phys. Rev. D* **90**, 013001 (2014), arXiv:1405.1935 [hep-ph].
- [37] P. Touboul *et al.*, “MICROSCOPE Mission: First Results of a Space Test of the Equivalence Principle,” *Phys. Rev. Lett.* **119**, 231101 (2017), arXiv:1712.01176 [astro-ph.IM].
- [38] J. Bergé, P. Brax, G. Métris, M. Pernot-Borràs, P. Touboul, and J.-P. Uzan, “MICROSCOPE Mission: First Constraints on the Violation of the Weak Equivalence Principle by a Light Scalar Dilaton,” *Phys. Rev. Lett.* **120**, 141101 (2018), arXiv:1712.00483 [gr-qc].
- [39] P. Touboul *et al.* (MICROSCOPE), “MICROSCOPE Mission: Final Results of the Test of the Equiva-

- lence Principle,” *Phys. Rev. Lett.* **129**, 121102 (2022), [arXiv:2209.15487 \[gr-qc\]](#).
- [40] D. W. P. Amaral, M. Jain, M. A. Amin, and C. Tunnel, “Vector Wave Dark Matter and Terrestrial Quantum Sensors,” (2024), [arXiv:2403.02381 \[hep-ph\]](#).
- [41] T. A. Wagner, S. Schlamminger, J. H. Gundlach, and E. G. Adelberger, “Torsion-balance tests of the weak equivalence principle,” *Class. Quant. Grav.* **29**, 184002 (2012), [arXiv:1207.2442 \[gr-qc\]](#).
- [42] C. O’Hare, “cajohare/axionlimits: Axionlimits,” <https://cajohare.github.io/AxionLimits/> (2020).
- [43] R. Abbott *et al.* (LIGO Scientific, KAGRA, Virgo), “Constraints on dark photon dark matter using data from LIGO’s and Virgo’s third observing run,” *Phys. Rev. D* **105**, 063030 (2022), [arXiv:2105.13085 \[astro-ph.CO\]](#).
- [44] A. G. Abac *et al.* (LIGO Scientific, VIRGO, KAGRA), “Ultralight vector dark matter search using data from the KAGRA O3GK run,” (2024), [arXiv:2403.03004 \[astro-ph.CO\]](#).
- [45] P. W. Graham, D. E. Kaplan, J. Mardon, S. Rajendran, and W. A. Terrano, “Dark Matter Direct Detection with Accelerometers,” *Phys. Rev. D* **93**, 075029 (2016), [arXiv:1512.06165 \[hep-ph\]](#).
- [46] D. Carney *et al.*, “Mechanical Quantum Sensing in the Search for Dark Matter,” *Quantum Sci. Technol.* **6**, 024002 (2021), [arXiv:2008.06074 \[physics.ins-det\]](#).
- [47] D. Carney, A. Hook, Z. Liu, J. M. Taylor, and Y. Zhao, “Ultralight dark matter detection with mechanical quantum sensors,” *New J. Phys.* **23**, 023041 (2021), [arXiv:1908.04797 \[hep-ph\]](#).
- [48] J. Manley, M. D. Chowdhury, D. Grin, S. Singh, and D. J. Wilson, “Searching for vector dark matter with an optomechanical accelerometer,” *Phys. Rev. Lett.* **126**, 061301 (2021), [arXiv:2007.04899 \[quant-ph\]](#).
- [49] M. Abe, P. Adamson, M. Borcean, D. Bortoletto, K. Bridges, S. P. Carman, S. Chattopadhyay, J. Coleman, N. M. Curfman, K. DeRose, *et al.*, “Matter-wave atomic gradiometer interferometric sensor (magis-100),” *Quantum Science and Technology* **6**, 044003 (2021).
- [50] A. Pierce, K. Riles, and Y. Zhao, “Searching for Dark Photon Dark Matter with Gravitational Wave Detectors,” *Phys. Rev. Lett.* **121**, 061102 (2018), [arXiv:1801.10161 \[hep-ph\]](#).
- [51] S. Morisaki, T. Fujita, Y. Michimura, H. Nakatsuka, and I. Obata, “Improved sensitivity of interferometric gravitational wave detectors to ultralight vector dark matter from the finite light-traveling time,” *Phys. Rev. D* **103**, L051702 (2021), [arXiv:2011.03589 \[hep-ph\]](#).
- [52] H. Nakatsuka, S. Morisaki, T. Fujita, J. Kume, Y. Michimura, K. Nagano, and I. Obata, “Stochastic effects on observation of ultralight bosonic dark matter,” (2022), [arXiv:2205.02960 \[astro-ph.CO\]](#).
- [53] M. A. Fedderke and A. Mathur, “Asteroids for ultralight dark-photon dark-matter detection,” *Phys. Rev. D* **107**, 043004 (2023), [arXiv:2210.09324 \[hep-ph\]](#).
- [54] A. Vinante, P. Falferi, G. Gasbarri, A. Setter, C. Timberlake, and H. Ulbricht, “Ultralow mechanical damping with meissner-levitated ferromagnetic microparticles,” *Phys. Rev. Appl.* **13**, 064027 (2020).
- [55] J. Hofer, R. Gross, G. Higgins, H. Huebl, O. F. Kieler, R. Kleiner, D. Koelle, P. Schmidt, J. A. Slater, M. Trupke, K. Uhl, T. Weimann, W. Wiczorek, and M. Aspelmeyer, “High- q magnetic levitation and control of superconducting microspheres at millikelvin temperatures,” *Phys. Rev. Lett.* **131**, 043603 (2023).
- [56] P. Schmidt *et al.*, “Remote sensing of a levitated superconductor with a flux-tunable microwave cavity,” *Phys. Rev. Applied* **22**, 014078 (2024), [arXiv:2401.08854 \[quant-ph\]](#).
- [57] T. M. Fuchs, D. G. Uitenbroek, J. Plugge, N. van Halteren, J.-P. van Soest, A. Vinante, H. Ulbricht, and T. H. Oosterkamp, “Measuring gravity with milligram levitated masses,” (2023), [arXiv:2303.03545 \[quant-ph\]](#).
- [58] M. Janse, D. G. Uitenbroek, L. van Everdingen, J. Plugge, B. Hensen, and T. H. Oosterkamp, “Current experimental upper bounds on spacetime diffusion,” *Phys. Rev. Res.* **6**, 033076 (2024), [arXiv:2403.08912 \[quant-ph\]](#).
- [59] G. Higgins, S. Kalia, and Z. Liu, “Maglev for dark matter: Dark-photon and axion dark matter sensing with levitated superconductors,” *Phys. Rev. D* **109**, 055024 (2024), [arXiv:2310.18398 \[hep-ph\]](#).
- [60] R. Li, S. Lin, L. Zhang, C. Duan, P. Huang, and J. Du, “Search for Ultralight Dark Matter with a Frequency Adjustable Diamagnetic Levitated Sensor,” *Chin. Phys. Lett.* **40**, 069502 (2023), [arXiv:2307.15758 \[astro-ph.CO\]](#).
- [61] S. Kalia, D. Budker, D. F. J. Kimball, W. Ji, Z. Liu, A. O. Sushkov, C. Timberlake, H. Ulbricht, A. Vinante, and T. Wang, “Ultralight dark matter detection with levitated ferromagnets,” (2024), [arXiv:2408.15330 \[hep-ph\]](#).
- [62] R. Catena and P. Ullio, “A novel determination of the local dark matter density,” *JCAP* **08**, 004 (2010), [arXiv:0907.0018 \[astro-ph.CO\]](#).
- [63] J. I. Read, “The Local Dark Matter Density,” *J. Phys. G* **41**, 063101 (2014), [arXiv:1404.1938 \[astro-ph.GA\]](#).
- [64] N. W. Evans, C. A. J. O’Hare, and C. McCabe, “Refinement of the standard halo model for dark matter searches in light of the Gaia Sausage,” *Phys. Rev. D* **99**, 023012 (2019), [arXiv:1810.11468 \[astro-ph.GA\]](#).
- [65] See Supplemental Material.
- [66] J. W. Foster, N. L. Rodd, and B. R. Safdi, “Revealing the Dark Matter Halo with Axion Direct Detection,” *Phys. Rev. D* **97**, 123006 (2018), [arXiv:1711.10489 \[astro-ph.CO\]](#).
- [67] G. P. Centers *et al.*, “Stochastic fluctuations of bosonic dark matter,” *Nature Commun.* **12**, 7321 (2021), [arXiv:1905.13650 \[astro-ph.CO\]](#).
- [68] M. Lisanti, M. Moschella, and W. Terrano, “Stochastic properties of ultralight scalar field gradients,” *Phys. Rev. D* **104**, 055037 (2021), [arXiv:2107.10260 \[astro-ph.CO\]](#).
- [69] B. van Heck, T. M. Fuchs, J. Plugge, W. A. Bosch, and T. H. Oosterkamp, “Magnetic Cooling and Vibration Isolation of a Sub-kHz Mechanical Resonator,” *J. Low Temp. Phys.* **210**, 588 (2023), [arXiv:2208.11750 \[quant-ph\]](#).
- [70] C. Timberlake, G. Gasbarri, A. Vinante, A. Setter, and H. Ulbricht, “Acceleration sensing with magnetically levitated oscillators above a superconductor,” *Appl. Phys. Lett.* **115**, 224101 (2019), [arXiv:1910.07078 \[physics.app-ph\]](#).
- [71] M. Mück, J. Kycia, and J. Clarke, “Superconducting quantum interference device as a near-quantum-limited amplifier at 0.5 ghz,” *Applied Physics Letters* **78**, 967 (2001).
- [72] B. van Waarde, O. Benningshof, and T. Oosterkamp, “A Magnetic Persistent Current Switch at milliKelvin Temperatures,” *Cryogenics* **78**, 74 (2016), [arXiv:1601.02439 \[physics.ins-det\]](#).

- [73] M. Maggiore *et al.*, “Science Case for the Einstein Telescope,” *JCAP* **03**, 050 (2020), [arXiv:1912.02622 \[astro-ph.CO\]](#).
- [74] E. J. Groth, “Probability distributions related to power spectra.” *Astrophysical Journal, Suppl. Ser.*, Vol. 29, No. 286, p. 285-302 **29**, 285 (1975).
- [75] G. Cowan, K. Cranmer, E. Gross, and O. Vitells, “Asymptotic formulae for likelihood-based tests of new physics,” *Eur. Phys. J. C* **71**, 1554 (2011), [Erratum: *Eur.Phys.J.C* 73, 2501 (2013)], [arXiv:1007.1727 \[physics.data-an\]](#).

Ultralight $B - L$ Dark Matter

The Lagrangian for a new, massive gauge field that couples to the difference between the baryon and lepton number, $B - L$, reads

$$\mathcal{L} \supset -\frac{\varepsilon_0 c^2}{4} A^{\mu\nu} A_{\mu\nu} + \frac{\varepsilon_0}{2} \left(\frac{m_{A'} c^2}{\hbar} \right)^2 A^\mu A_\mu - g_{B-L} j_{B-L}^\mu A_\mu, \quad (7)$$

where $A^{\mu\nu} \equiv \partial^\mu A^\nu - \partial^\nu A^\mu$ is the field strength tensor for the new field, m_A is the mass of the field, and j_{B-L}^μ is the $B - L$ vector current. Since we take this field to be dark matter, we equate $m_A = m_{\text{DM}}$. The vector current is given by

$$j_{B-L}^\mu = \sum_f Q_{B-L}^f \bar{f} \gamma^\mu f, \quad (8)$$

where the sum runs over all fermions in the Standard Model, and Q_{B-L}^f is the $B - L$ charge of fermion f .

In the ultralight regime, we can write the dark matter field at time t and position \mathbf{x} as [40]

$$\mathbf{A}(\mathbf{x}, t) = |\mathbf{A}| \text{Re} \left\{ \frac{1}{\sqrt{V}} \sum_{\mathbf{k}} \sqrt{f_{\mathbf{k}}} e^{-i(\omega_{\text{DM}}^{\mathbf{k}} t + \mathbf{k} \cdot \mathbf{x})} \boldsymbol{\epsilon}_{\mathbf{k}} \right\}, \quad (9)$$

where the sum runs over the possible wavevectors of the field, $\mathbf{k} = m_{\text{DM}} \mathbf{v} / \hbar$ (which are dictated by the Milky Way halo distribution $f_{\mathbf{k}}$), the angular velocity of the field is given by $\omega_{\text{DM}}^{\mathbf{k}} \equiv m_{\text{DM}} c^2 / \hbar + \hbar^2 |\mathbf{k}|^2 / (2m_{\text{DM}})$, and $\boldsymbol{\epsilon}_{\mathbf{k}}$ is a random variable encoding the phases of the field at each wavevector. The volume factor $V^{-1/2}$ appears as we have discretized the field. The halo distribution function is given by

$$f_{\mathbf{k}} \equiv \mathcal{N} \exp \left(-\frac{|\mathbf{k} - \bar{\mathbf{k}}|^2}{2k_0^2} \right) \quad \text{with} \quad \frac{\mathcal{N}}{V} \sum_{\mathbf{k}} f_{\mathbf{k}} = 1, \quad (10)$$

where $k_0 \equiv m_{\text{DM}} v_0 / \hbar$ is the wavevector of the field at the virial velocity v_0 .

In the coherent regime, where the observation time is much shorter than the dark matter coherence time $\tau_{\text{coh}} \equiv \lambda_{\text{dB}} / v_0 = \hbar / (m_{\text{DM}} v_0^2)$, we can neglect the kinetic term in $\omega_{\text{DM}}^{\mathbf{k}}$, such that $\omega_{\text{DM}}^{\mathbf{k}} \simeq \omega_{\text{DM}} \equiv m_{\text{DM}} c^2$. Moreover, since spatial variations in the field occur at the scale λ_{dB} , which is smaller than either the separation between our trap and levitated particle or the distance the Earth covers in its orbit during our measurement time, we set $\mathbf{x} = \mathbf{0}$ assuming statistical homogeneity of the field. This simplifies the expression for the field in Eq. (9) to

$$\mathbf{A}(t) \simeq |\mathbf{A}| \sum_i \alpha_i \cos(\omega_{\text{DM}} t + \varphi_i) \hat{\mathbf{e}}_i, \quad (11)$$

where the sum runs over $i \in \{x, y, z\}$, $\hat{\mathbf{e}}_i$ are the Cartesian unit basis vectors, and where the quantities α_i and

φ_i are random variables describing the amplitude and phase of the dark matter field, respectively. The three independent α_i follow Rayleigh distributions with variance $1/2$, and the three independent phases φ_i follow uniform distributions from 0 to 2π :

$$p(\alpha_i) = 2\alpha_i e^{-\alpha_i^2} \quad \text{and} \quad p(\varphi_i) = \frac{1}{2\pi}. \quad (12)$$

Further details and derivations of the above can be found in Ref. [40].

Equating the energy density of the field to that of dark matter sets the normalization of the field. In the non-relativistic regime, we have that

$$\frac{\varepsilon_0}{2} \left[\langle |\dot{\mathbf{A}}|^2 \rangle + \left(\frac{m_{\text{DM}} c^2}{\hbar} \right)^2 \langle |\mathbf{A}|^2 \rangle \right] = \rho_{\text{DM}}. \quad (13)$$

From Eq. (11) and Eq. (12), we can compute all relevant expectation values. This gives us

$$|\mathbf{A}| = \frac{\hbar}{m_{\text{DM}} c^2} \sqrt{\frac{2\rho_{\text{DM}}}{3\varepsilon_0}}, \quad (14)$$

To make contact with our experiment, we can derive the force that the new gauge field imparts on any object charged under it. This force will take the form of a new Lorentz force created by the electric and magnetic fields sourced by the new gauge field, \mathbf{E} and \mathbf{B} respectively. Writing $A^\mu \equiv (\phi/c, \mathbf{A})$, where ϕ and \mathbf{A} are respectively the new scalar and vector potentials, we have that

$$\mathbf{E} = -\nabla\phi - \frac{\partial \mathbf{A}}{\partial t} \quad \text{and} \quad \mathbf{B} = \nabla \times \mathbf{A}. \quad (15)$$

While the temporal derivative picks out a factor of $\omega_{\text{DM}} \propto c^2$, the spatial derivatives lead to factors of $|\mathbf{k}| \propto v_0$. Since $v_0 \sim 10^{-3}c$, terms involving spatial derivatives are suppressed compared to the temporal derivative term, such that the dark magnetic field is negligible. Moreover, in the Lorenz gauge ($\partial_\mu A^\mu = 0$), the scalar potential is also suppressed compared to the vector potential by a factor of v_0 . Thus, we only need to consider the electric field produced by the dark matter field. Given a macroscopic, neutral object of total mass m , its net $B - L$ charge will be the total number of neutrons within it. We can therefore write the total force that the ultralight DM field should impart on an object as

$$\mathbf{F}(t) = g_{B-L} \mathcal{R} m a_0 \sum_i \alpha_i \cos(\omega_{\text{DM}} t + \varphi_i) \mathbf{e}_i, \quad (16)$$

where we have absorbed an irrelevant phase of $\pi/2$ into each φ_i . We have also defined the ratio of neutrons to atomic mass as $\mathcal{R} \equiv N/A$ and the acceleration given per nucleon as

$$a_0 \equiv \frac{1}{u} \sqrt{\frac{2e^2 \rho_{\text{DM}}}{3\varepsilon_0}} \approx 2.12 \times 10^{11} \text{ m s}^{-2}, \quad (17)$$

where $u \approx 1.66 \times 10^{-27} \text{ kg}$ is the atomic mass unit and the DM energy density is $\rho_{\text{DM}} \approx 0.4 \text{ GeV}/c^2 \text{ cm}^{-3}$ [63].

Dark Matter Force Signal

The total vector force imparted by the ultralight DM field onto an object is given by Eq. (16). To simplify our analysis, we only consider the motion of the particle along a single direction. Arbitrarily, we choose this to point along the North-South line; ultimately, this choice has no impact on our results. We can then write our sensitivity axis as

$$\begin{aligned} \zeta &\equiv (\cos \lambda \cos(\omega_{\oplus} t + \phi), \cos \lambda \sin(\omega_{\oplus} t + \phi), \sin \lambda)^{\top} \\ &\simeq (\cos \lambda \cos \phi, \cos \lambda \sin \phi, \sin \lambda)^{\top}, \end{aligned} \quad (18)$$

where λ and ϕ are the latitude and longitude of our experiment, respectively, and ω_{\oplus} is the angular frequency of a sidereal day, $\omega_{\oplus} = 2\pi/T_{\oplus} \approx 7.5 \times 10^{-5}$ Hz. Since our total observation times are always significantly shorter than a day, we make the approximation that $\omega_{\oplus} t \ll 1$, which we have checked to be appropriate. The relevant force experienced by an object is then

$$\begin{aligned} F_{\text{DM}}(t) &\equiv \zeta \cdot \mathbf{F}(t) \\ &= g_{B-L} \mathcal{R} m a_0 [\alpha_x \cos \lambda \cos \phi \cos(\omega_{\text{DM}} t + \varphi_x) \\ &\quad + \alpha_y \cos \lambda \sin \phi \cos(\omega_{\text{DM}} t + \varphi_y) \\ &\quad + \alpha_z \sin \lambda \cos(\omega_{\text{DM}} t + \varphi_z)]. \end{aligned} \quad (19)$$

The dynamics of our system can be modelled as two coupled springs in the weak coupling limit. The equations of motion describing the trap and levitated particle along our axis of sensitivity are then, respectively,

$$\begin{aligned} \ddot{x}_t + \gamma_t \dot{x}_t + \omega_t^2 x_t &= \frac{F_{\text{DM}}^t(t)}{m_t}, \\ \ddot{x}_p + \gamma_p \dot{x}_p + \omega_p^2 (x_p - x_t) &= \frac{F_{\text{DM}}^p(t)}{m_p}, \end{aligned} \quad (20)$$

where $\gamma_i \equiv \omega_i/Q_i$ are the thermal dissipation rates, with ω_i and Q_i the resonance angular frequencies and quality factors of the respective parts of the setup. We have indicated this via t and p , stipulating that we are considering either trap or particle. From this system of equations, we can solve for the trap dynamics separately and then use this solution to solve for the levitated particle dynamics.

For a sinusoidal driving force of the form $F(t) \equiv F_0 \cos(\omega t + \varphi)$, the solution to the driven-damped harmonic oscillator can be written as

$$x(t) = |\chi(\omega)| F_0 \cos[\omega t + \varphi - \arg(\chi(\omega))], \quad (21)$$

where the transfer function $\chi(\omega)$ is given by

$$\chi(\omega) \equiv \frac{1}{m(\omega_0^2 - \omega^2 + i\gamma\omega)}. \quad (22)$$

Assuming the trap to have a resonance frequency far below the DM driving frequency, the trap dynamics follow

$$x_t(t) = -\frac{F_{\text{DM}}^t(t)}{m_t \omega_{\text{DM}}^2}. \quad (23)$$

Inserting this into the equation of motion for the levitated particle, we can read off the total force experienced by it:

$$\begin{aligned} F_{\text{DM}}^p(t) &= \mathcal{F}[\alpha_x \cos \lambda \cos \phi \cos(\omega_{\text{DM}} t + \varphi_x) \\ &\quad + \alpha_y \cos \lambda \sin \phi \cos(\omega_{\text{DM}} t + \varphi_y) \\ &\quad + \alpha_z \sin \lambda \cos(\omega_{\text{DM}} t + \varphi_z)], \end{aligned} \quad (24)$$

where we have defined the quantity

$$\mathcal{F} = g_{B-L} \left(\mathcal{R}_p - \frac{\omega_0^2}{\omega_{\text{DM}}^2} \mathcal{R}_t \right) m_p a_0. \quad (25)$$

This is the form of the force we use in Eq. (2), where we have made the notational replacement $\omega_p \rightarrow \omega_0$.

The total, random force experienced by the levitated particle can be decomposed into the driving dark matter force above and forces stemming from environmental noise,

$$F_p(t) = F_{\text{DM}}^p(t) + F_{\text{noise}}^p(t), \quad (26)$$

We assume that the noise is white, such that it has equal power across all frequencies. For white noise, the force should be normally distributed as $F_{\text{noise}}^p \sim \mathcal{N}(0, \sigma^2)$, where $\sigma^2 \equiv S_{FF}(\omega) \Delta f$ is the force noise variance in the time domain, $S_{FF}(\omega)$ is the force noise power spectral density (PSD), and Δf is the sampling frequency.

We can derive the expected (one-sided) signal PSD using the discrete Fourier transform,

$$\mathcal{P}(\omega) \equiv 2 \frac{(\Delta t)^2}{T_{\text{obs}}} \left| \sum_{n=0}^{N-1} F_p(t_n) e^{i\omega n \Delta t} \right|^2, \quad (27)$$

where ω is the angular frequency, N is the number of points sampled in the time domain, and $\Delta t \equiv T_{\text{obs}}/N$ is the sampling frequency, with T_{obs} the total observation time. The factor of two accounts for the ‘folding’ of the result from negative angular frequencies to positive angular frequencies to produce the one-sided periodogram.

From this, we can derive an expression for the signal periodogram normalised by the expected force noise PSD, S_{FF} . We call this quantity the excess power, Λ . Defining the dimensionless parameter

$$\kappa \equiv \sqrt{\frac{\mathcal{F}^2 T_{\text{obs}}}{2 S_{FF}}}, \quad (28)$$

we have that

$$\begin{aligned} \Lambda(\kappa, \boldsymbol{\alpha}, \boldsymbol{\varphi}; \omega) &\equiv \frac{\mathcal{P}(\omega)}{S_{FF}(\omega)} \\ &= \kappa^2 [\alpha_x^2 \cos^2 \lambda \cos^2 \phi + \alpha_y^2 \cos^2 \lambda \sin^2 \phi + \alpha_z^2 \sin^2 \lambda \\ &\quad + 2\alpha_x \alpha_y \cos^2 \lambda \sin \phi \cos \phi \cos(\varphi_y - \varphi_x) \\ &\quad + 2\alpha_x \alpha_z \sin \lambda \cos \lambda \cos \phi \cos(\varphi_z - \varphi_x) \\ &\quad + 2\alpha_y \alpha_z \sin \lambda \cos \lambda \sin \phi \cos(\varphi_z - \varphi_y)] \delta_{\omega, \omega_{\text{DM}}}, \end{aligned} \quad (29)$$

This expression is similar to that derived in Ref. [40]; however, their observation time was taken to be longer than a sidereal day, leading to three peaks instead of one.

Statistical Analysis

Derivation of Likelihood Function

For a monochromatic signal such as the one we expect from ULDM, the measured excess power in the bin containing the signal, p , should be distributed according to a non-central χ^2 distribution with two degrees of freedom and non-centrality parameter Λ given by Eq. (29) [40, 74]. To account for the stochastic ULDM variables, we define the marginalized likelihood

$$\mathcal{L}(\kappa; p) \equiv \int \chi^2(p; 2, \Lambda(\kappa, \boldsymbol{\alpha}, \boldsymbol{\varphi})) \pi(\boldsymbol{\alpha}, \boldsymbol{\varphi}) d^3\boldsymbol{\alpha} d^3\boldsymbol{\varphi}, \quad (30)$$

where $\pi(\boldsymbol{\alpha}, \boldsymbol{\varphi})$ is the joint probability density of the Rayleigh amplitudes and uniformly distributed phases of the ULDM field. Individually, these random variables follow the probability densities given in Eq. (12). Since each of them is statistically independent, their joint probability density is the product of their individual densities. We assume that they take constant values over a coherence time, simplifying the theoretical hurdle of modelling their continuous change while still allowing us to account for their randomness in our statistical treatment.

We can perform a change of variables from the above polar space to a Cartesian one. The random amplitudes and phases can then be described by the three random vectors $\boldsymbol{x} \equiv (x_1, x_2)^\top$, $\boldsymbol{y} \equiv (y_1, y_2)^\top$, and $\boldsymbol{z} \equiv (z_1, z_2)^\top$. Each component of \boldsymbol{x} , \boldsymbol{y} , and \boldsymbol{z} then has a mean of zero, with variances of $\cos^2 \lambda \cos^2 \phi/2$, $\cos^2 \lambda \sin^2 \phi/2$, and $\sin^2 \lambda/2$, respectively. In this basis, the non-centrality parameter can be compactly written as

$$\Lambda(\kappa) = \kappa^2 |\boldsymbol{x} + \boldsymbol{y} + \boldsymbol{z}|^2. \quad (31)$$

It is convenient to perform one further change of variables to $\boldsymbol{u} \equiv \boldsymbol{x} + \boldsymbol{y} + \boldsymbol{z}$, $\boldsymbol{v} \equiv \boldsymbol{x} + \boldsymbol{y} - \boldsymbol{z}$, and $\boldsymbol{w} \equiv \boldsymbol{x} - \boldsymbol{y} - \boldsymbol{z}$. The last two definitions are required to complete our transformation. Each component of these vectors is now normally distributed with zero mean and variance $1/2$. The joint probability density then transforms as $\pi(\boldsymbol{\alpha}, \boldsymbol{\varphi}) d^3\boldsymbol{\alpha} d^3\boldsymbol{\varphi} \rightarrow \pi'(\boldsymbol{u}, \boldsymbol{v}, \boldsymbol{w}) d^2\boldsymbol{u} d^2\boldsymbol{v} d^2\boldsymbol{w}$, with

$$\pi'(\boldsymbol{u}, \boldsymbol{v}, \boldsymbol{w}) = \frac{1}{\pi^3} e^{-|\boldsymbol{u}|^2} e^{-|\boldsymbol{v}|^2} e^{-|\boldsymbol{w}|^2}. \quad (32)$$

In this basis, we can expand the non-central χ^2 distribution in terms of the modified Bessel function, I_0 , to write the likelihood in Eq. (30) as

$$\mathcal{L}(\kappa; p) = \frac{e^{-p/2}}{2} \sum_{n=0}^{\infty} \frac{p^n}{(2^n n!)^2} \mathcal{I}_n(\kappa), \quad (33)$$

with the integral $\mathcal{I}_n(\kappa)$ given by

$$\mathcal{I}_n(\kappa) \equiv \int e^{-\frac{\kappa^2 |\boldsymbol{u}|^2}{2}} (\kappa |\boldsymbol{u}|)^{2n} \pi' d^2\boldsymbol{u} d^2\boldsymbol{v} d^2\boldsymbol{w}. \quad (34)$$

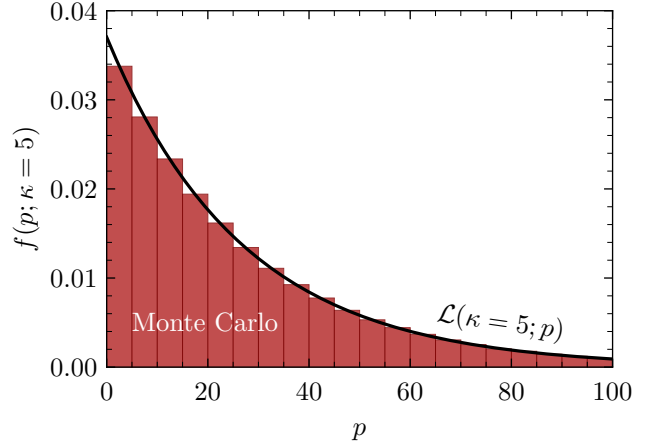


FIG. 5: Distribution of the measured excess power p in the coherent regime for $\kappa = 5$ (see Eq. (4)). Data was simulated from 10^6 Monte Carlo runs beginning from Eq. (2). The solid line shows the analytical result of Eq. (30) and is in excellent agreement with simulations.

We can analytically evaluate this using the integral definition of the gamma function, yielding

$$\mathcal{I}_n(\kappa) = \frac{2\kappa^{2n} (2^n n!)}{(2 + \kappa^2)^{n+1}}. \quad (35)$$

Substituting this into Eq. (33), we arrive at our result:

$$\mathcal{L}(\kappa; p) = \frac{1}{2 + \kappa^2} e^{-p/(2 + \kappa^2)}. \quad (36)$$

This likelihood suggests that the statistics of our problem do not depend on the positional parameters λ and ϕ . This is because our observation times are shorter than the sidereal period of the Earth, such that we treat our detector as being effectively stationary. Since the ULDM field is isotropic, with each random variable being identically and independently distributed, it should not matter where on Earth we are when making inferences. Thus, while the measured force and periodogram do depend on our position, statistical conclusions do not.

We verify this likelihood using Monte Carlo simulations. We generate 10^6 force signals according to Eq. (2) in the time domain, arbitrarily taking the DM angular frequency to be $\omega_{\text{DM}} = 2\pi$ Hz, with $\mathcal{F} = 5$ N, $T_{\text{obs}} = 10$ s, $\lambda = 45^\circ$, $\phi = 30^\circ$, and $\sigma^2 = 5 \text{ N}^2 \text{ Hz}^{-1}$, giving $\kappa = 5$. In each simulation, we draw α and φ from the distributions shown in Eq. (12). Finally, we take the one-sided PSD using the discrete Fourier transform in Eq. (27). We show the distribution of the excess power p in the signal-containing bin in Fig. 5. We find excellent agreement with our derived likelihood.

Inferencing Framework

To perform our inferences, we use the likelihood ratio

$$\tilde{\lambda}(\kappa) \equiv \begin{cases} \frac{\mathcal{L}(\kappa; p)}{\mathcal{L}(\hat{\kappa}; p)} & \text{if } \hat{\kappa} \geq 0, \\ \frac{\mathcal{L}(\kappa; p)}{\mathcal{L}(0; p)} & \text{else.} \end{cases} \quad (37)$$

The parameter $\hat{\kappa}$ is the maximum-likelihood estimator of κ , maximising the likelihood given the measured value of the excess power p . The piecewise condition captures the physicality of the parameter κ : if $\hat{\kappa}$ falls outside of its physical domain of $\kappa \in [0, \infty)$, $\hat{\kappa}$ is set to 0. We then construct the two-sided test statistic (TS) [75]

$$\tilde{t}_\kappa \equiv -2 \ln \tilde{\lambda}(\kappa), \quad (38)$$

which is used to assess whether the null hypothesis, defined according to the likelihood in the numerator of Eq. (37), is a good description of the observed data compared to the alternative hypothesis, defined as per the maximised unconditional likelihood. A value of 0 for \tilde{t}_κ indicates perfect agreement with the null hypothesis, with larger values indicating greater disagreement.

To reject the null hypothesis, we define a value for the test statistic that is deemed too extreme to have come from that model. Specifically, if $f(\tilde{t}_\kappa|\kappa)$ is the distribution of \tilde{t}_κ values that we would expect to arise from the null hypothesis defined by the parameter κ , then we can define the p -value of the observed \tilde{t}_κ , $\tilde{t}_\kappa^{\text{obs}}$, as

$$p_\kappa \equiv \int_{\tilde{t}_\kappa^{\text{obs}}}^{\infty} f(\tilde{t}_\kappa|\kappa) d\tilde{t}_\kappa, \quad (39)$$

telling us how probable it is for us to have observed a value of \tilde{t}_κ at least as extreme as $\tilde{t}_\kappa^{\text{obs}}$. We find $f(\tilde{t}_\kappa|\kappa)$ from a series of Monte Carlo (MC) simulations, generating 10^6 pseudo-datasets distributed according to the likelihood given in Eq. (36) for each value of κ begin tested. For each pseudo-dataset, we then compute the value of \tilde{t}_κ from Eq. (38). The distribution of these values is $f(\tilde{t}_\kappa|\kappa)$.

To assess the discovery significance of our data, we consider p_0 . We first compute the value of the excess power $p = \mathcal{P}/S_{FF}$ within every frequency bin, where S_{FF} given by the fit in Eq. (6) and shown in Fig. 2 along with our data, \mathcal{P} . We then compute the value of \tilde{t}_0 within each bin. We find our lowest local value to be $p_0 \approx 2.0 \times 10^{-2}$, an order of magnitude greater our preset condition for discovery, set at the *local* p -value of $p_0 \approx 2.7 \times 10^{-3}$ for a 3σ significance. We therefore cannot claim a discovery and turn to the task of limit setting.

We proceed similarly to compute our 90% confidence level (CL) limits. We define the false positive rate as $\alpha = 0.1$ and find that value of κ , κ_{lim} , for which $p_\kappa = \alpha$ within each frequency bin. We use our measured PSD for our data-driven limit, whereas we assume that we observe background-only data for our expected upper

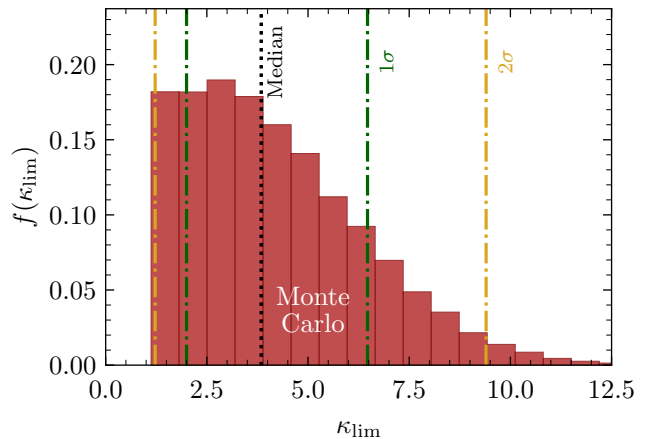


FIG. 6: Distribution of 90% confidence level limits on κ derived from our Monte Carlo procedure. The median value is given by $\kappa_{\text{lim}}^{\text{med}} \approx 3.85$, and the 1σ and 2σ bands are given by $\kappa_{\text{lim}}^{1\sigma} \in [2.01, 6.47]$ and $\kappa_{\text{lim}}^{2\sigma} \in [1.23, 9.39]$, respectively.

limits. For the latter, we generate 10^6 background-only pseudo-datasets according to Eq. (36) with $\kappa = 0$. For each of these datasets, we find κ_{lim} , producing a distribution of κ_{lim} values, shown in Fig. 6. We derive a median value of $\kappa_{\text{lim}}^{\text{med}} \approx 3.85$, with 1σ and 2σ bands respectively given by $\kappa_{\text{lim}}^{1\sigma} \in [2.01, 6.47]$ and $\kappa_{\text{lim}}^{2\sigma} \in [1.23, 9.39]$. To find the corresponding quantities for g_{B-L} , we use Eq. (5). While the two-sided TS construction in Eq. (38) generally leads to two-sided limits, we only show the upper limits since we cannot claim discovery.

Future Experiments

We have three main sources of force noise: external vibrations, thermal noise from the environment that is at some equilibrium temperature and to which the particle is coupled through the dissipation of its mechanical motion, and backaction noise arising from the measurement of the particle position. Currently, we are limited by external vibrations, and therefore any improvements in vibration isolation will improve our force sensitivity. At our present resonance frequency, we have vibration isolation at the level of 80 dB. At the current Q factor of the resonator, we will need to improve this isolation by roughly 20 dB to reach thermal motion at 50 mK. As the Q factor increases or temperature decreases, the vibration isolation will need to be improved as $(Q/T)^{1/2}$, equivalent to 10 dB for every factor order of magnitude increase in Q or decrease in temperature. Moreover, for every order of magnitude increase in the particle mass, we will need to improve this isolation by 20 dB. We note that vibration isolation typically works better at higher frequencies.

For the backaction noise, the position of the magnetic particle is first converted to a flux in a pick-up coil, and this flux is subsequently measured with a SQUID. The backaction noise then arises from the current noise in the SQUID, which couples back as a current noise in the pick-up coil, exerting a force on the particle. The parameter needed to quantify the amount of backaction noise is the energy coupling, $\beta^2 \equiv L_{\text{tot}} I^2 / (m_p v_p^2)$, which is the ratio between the induction energy produced by the currents in the superconducting circuit due to the motion of the particle and the kinetic energy of the particle. The backaction force is then determined by the SQUID noise, $S_{\Phi\Phi}$. At a given energy coupling, SQUID noise, and Q factor, we can calculate the minimum temperature T of the experiment below which the backaction of the SQUID becomes dominant over the thermal noise of the experiment. This occurs when

$$4k_B T \frac{m_p \omega_0}{Q} > k \beta^2 \frac{L_{\text{tot}}}{k_M^2 L_{\text{inp}}} 2n_{\text{SQ}} \hbar. \quad (40)$$

Here, m_p is the mass of the particle, ω_0 is its resonance frequency in the trap, Q is the quality factor, k is the spring constant, L_{tot} is the total inductance of the superconducting circuit, k_M is the mutual inductance coupling constant, L_{inp} is the SQUID input inductance, and n_{SQ} is the energy resolution of the SQUID. This energy resolution is given by $S_{\Phi\Phi} / (2L_{\text{SQ}}) = n_{\text{SQ}} \hbar$.

Force sensitivity is not the only thing to consider. To exclude ULDM over a larger frequency range than in Fig. 3, we must increase the bandwidth over which a resonator is sensitive. The detection noise has an important effect on the bandwidth of the experiment. Rather than the familiar ‘full-width half-maximum’ bandwidth, $\Delta f_{\text{FWHM}} \equiv f_0 / Q$, the detectable bandwidth is used. This is the bandwidth for which the position noise due to the fluctuations in the motion of the resonator is larger than the incorporated detection noise. This occurs at the bandwidth

$$\Delta f_{\text{det}} \equiv \frac{f_0}{Q} \sqrt{R_S - 1}, \quad (41)$$

where $R_S \equiv S_{xx, \text{motion}} / S_{xx, \text{SQ}} = S_{FF} \cdot |\chi(\omega_0)|^2 / S_{xx, \text{SQ}}$ is the ratio between the two contributions to the position noise. This relates the detectable bandwidth to the energy coupling, quality factor, temperature, and energy resolution of the SQUID. In the limit that the backaction noise dominates over the force noise, $R = Q^2 \beta^4$ and the bandwidth reduces to

$$\Delta f_{\text{opt}} = f_0 \beta_{\text{opt}}^2. \quad (42)$$

These factors, together with the particle mass, number of particles, and the difference between the neutron-to-atomic-weight ratios of the levitated particle and trap, are factors that dictate the short-, medium-, and long-term upgrades for our experiment.

When searching for ULDM at an unknown frequency, we would like to stress the importance of the bandwidth, which as implied by Eq. (42) grows with coupling β^2 . If we already the frequency at which to search for ULDM, we would choose the resonator’s resonance frequency to coincide with the frequency of the ULDM. Moreover, the bandwidth of the experiment would not be as important as long as it was larger than the bandwidth necessary to detect the time-varying amplitude and phase of the ULDM field. If the time scale at which amplitude and phase vary is of order 10^6 Compton cycles, then a bandwidth of the $f_0 / 10^6$ would suffice. This can be achieved using a coupling value of $\beta^2 \sim 10^{-6}$.

However, as long as the frequency is unknown, the optimal bandwidth depends on whether there is enough time available to spend 10^6 cycles at each frequency. If one wants to cover a large frequency in a limited amount of time, one could opt for a coupling larger than the optimal coupling, such as to have a larger bandwidth for each single experiment. This, however, comes at the expense of a larger backaction noise. On the one hand, this has the advantage that we need to do fewer experiments since, for a larger bandwidth per experiment, it takes fewer experiments to cover a full bandwidth. This comes at a cost because each of these experiments has a larger noise.

If the time to cover a full bandwidth is limited, the higher backaction noise is cancelled by the longer measurement time per frequency, and the limits are independent of Q and T . However if we can measure for a long time, such that one can wait for a set amount of cycles at each frequency, the noise is lowest for lower temperatures and higher Q factors. In the projections of Fig. 4, we decided on a total measurement time of two years with optimal coupling and 4.05×10^5 cycles at each frequency.

In Fig. 7, we plot the relevant quantities that we aim for in the short-, medium- and long-term scenarios. We believe the optimal β^2 can be reached since it is only a factor 10 to 100 larger than the β^2 in the realized experiment we analyzed. The detectable bandwidth then follows from β^2 . The force noise follows from the proposed parameters in Table I. The force noise is approximately 40 dB lower than the data presented. We believe this is achievable because we are currently limited by our vibration isolation system.

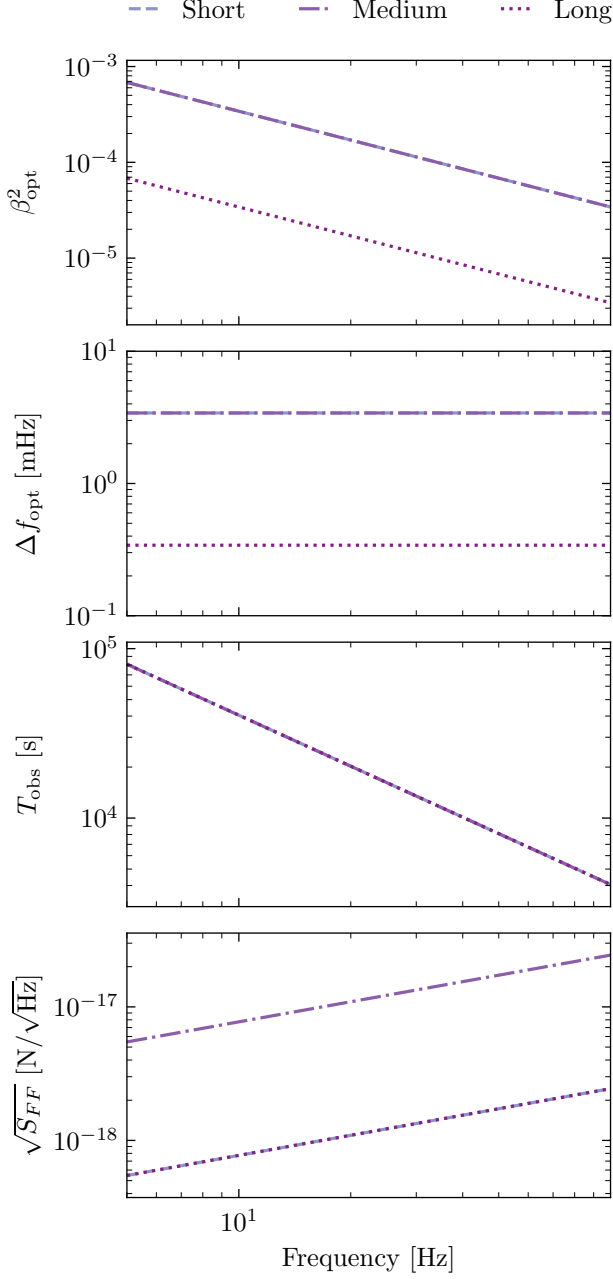


FIG. 7: Quantities needed to compute our projected limits in Fig. 4. These are the optimal SQUID coupling (β_{opt}^2), the optimal bandwidth that gives us equal thermal and backaction noise (Δf_{opt}), the observation time for 4.05×10^5 Compton cycles (T_{obs}), and the total root force noise PSD ($\sqrt{S_{FF}}$). The relevant parameters needed to compute these quantities are given in Table I.